Reducing tin droplet ejection from capillary porous structures under hydrogen plasma exposure in Magnum-PSI

Document Version:
Publisher's PDF, also known as Version of Record (includes final page, issue and volume numbers)

Please check the document version of this publication:

• A submitted manuscript is the version of the article upon submission and before peer-review. There can be important differences between the submitted version and the official published version of record. People interested in the research are advised to contact the author for the final version of the publication, or visit the DOI to the publisher's website.
• The final author version and the galley proof are versions of the publication after peer review.
• The final published version features the final layout of the paper including the volume, issue and page numbers.
Link to publication

Reducing tin droplet ejection from capillary porous structures under hydrogen plasma exposure in Magnum-PSI

J.G.A. Scholte [a,c,*], M. Iafrati [b], S.S.H. Lam [a], B. Tyburska-Pueschel [c], M. Riepen [d], F. Brochard [e], M.M.P. Vissers [a], T.W. Morgan [c,a]

[a] *Eindhoven University of Technology, De Zaale, Eindhoven, 5612AZ, The Netherlands*
[b] *ENEA Frascati Research Center, via Enerico Fermi 45, 00044, Frascati RM, Italy*
[c] *DIFFER-Dutch Institute for Fundamental Energy Research, De Zaale 20, 5612 AJ Eindhoven, The Netherlands*
[d] *ASML, De Run 6501, 5504 DR Veldhoven, The Netherlands*
[e] *Institut Jean Lamour, Université de Lorraine, UMR 7198 CNRS, 54011 Nancy Cede, France*

ARTICLE INFO

ABSTRACT

Liquid metal based divertors could be a more robust alternative to a solid tungsten design for DEMO. The liquid is confined in a sponge-like tungsten layer, called a capillary porous structure (CPS). It has been found previously that under certain conditions, many tin droplets eject from a CPS when it is brought into contact with a hydrogen plasma. These would present a contamination issue for the plasma core. Stability analysis suggests that droplet ejection can be suppressed by reduction of the pore size. To test this, stainless-steel CPS targets with pore size ranging from 0.5–100 μm filled with tin were exposed to identical loading conditions. This was done in the linear plasma device Magnum-PSI, capable of reaching divertor relevant plasma conditions. Furthermore, the influence of the CPS manufacturing techniques is considered by comparing the performance of a 3D printed, a mesh felts and a sintered CPS, all made from tungsten. Each target was surrounded by four witness plates, which were analysed post-mortem for Sn content by Rutherford backscattering. During plasma exposure, tin droplets were observed using a fast visible camera and plasma light emission via survey optical emission spectroscopy. The results imply that Sn erosion can be reduced by a factor of 50 when reducing the pore size. Moreover, it highlights the importance of avoiding overfilling of CPS targets with Sn.

1. Introduction

Several large steps in exhaust power and total loading fluences exist for the divertor design from ITER to DEMO, leading to an increased risk for a solid plasma facing component (PFC) design. This can potentially be mitigated utilizing a liquid metal based PFC. The neutron flux on the divertor increases more than one order of magnitude [1], leading to enhanced material damages [2]. For ITER, a major disruption, VDE [3] or unmitigated ELMs [4] could potentially melt tungsten. The increased fusion power in DEMO would only increase this risk [5,6]. In the current European DEMO design, the thickness of the W armour will be 8 mm, resulting in an expected lifetime of only 1.5 fpy, before it is eroded [1]. A liquid metal divertor (LMD) could be made thinner, as eroded material can be replenished by pumping fresh metal [7]. During off-normal events, vapour shielding protects the PFC [8]. Furthermore, collision cascades by neutrons do not lead to loss of performance, since a liquid lacks a crystal structure. Recent experimental progress in the study of liquid metals have been achieved on both linear plasma

devices [9–11] and tokamaks [12–15]. Proposed candidates for a liquid metal divertor (LMD) are lithium and tin, the relative merits of which are discussed in [16]. In this paper, the focus will be on tin.

A disadvantage of tin is its higher mass number. As a consequence, it could radiate more energy once it enters the plasma. Usually, the capillary action of a capillary porous structure (CPS) is used to keep the liquid in place [11,13,17]. Still, the liquid surface is not always stable and metal can be ejected from the surface when instabilities occur. Important sources are either due to the Kelvin–Helmholtz (KH) [10,18] or Raleigh–Taylor (RT) [19] instability. The former is due to the plasma shear, for which Miloshevsky and Hassenein [18] derived a theoretical model to predict the conditions necessary for a surface instability to materialize. In accordance, even an unbound liquid Sn surface should be stable [10] in the work of Ou [17] and in Magnum-PSI [20], as the rotational velocity due to the $\vec{E} \times \vec{B}$ force [21] is sufficiently small. RT instabilities can occur due to $\vec{j} \times \vec{B}$ forces, Jaworski [19] found the relationship between the critical current density and the

Table 1

Product information of the sintered s.s. discs, which all have a diameter of 25.4 mm. They were each wetted in a vacuum oven at the given temperatures and Sn amount. The porosity is determined by weighing the target before adding Sn, after filling it has been weighed again.

Pore size [µm]	Height [mm]	Mass [g]	Porosity	Max Sn [g]	Sn added [g]	T_{max} oven [°C]
0.5	1.58	4.932	0.217	1.253	0.796	950
1	1.60	4.793	0.260	1.547	1.070	900
2	1.64	4.472	0.323	1.963	1.341	900
5	1.68	4.530	0.330	2.048	1.336	900
10	1.66	4.168	0.376	2.307	1.335	900
20	1.68	3.925	0.419	2.604	1.349	900
40	3.12	7.195	0.428	4.956	3.717	950
100	3.34	5.035	0.621	7.588	4.633	950
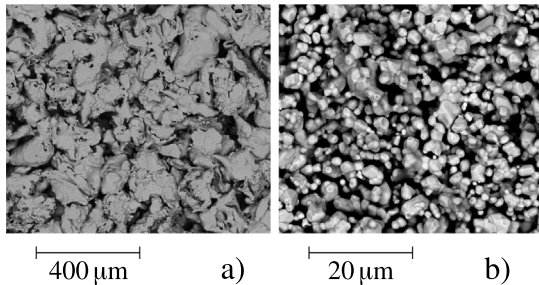
Fig. 1. SEM images of the (a) sintered s.s. target with a pore size of 5 µm and (b) sintered W disc. In the W disc the individual powder particles can be seen, while in the s.s. target the powder has fused into a larger structure.

magnetic field. However, Ou still found Sn droplets to be ejected from the surface of a CPS when exposed to a hydrogen plasma, which was not confined by a magnetic field. The formation and decomposition of stannane gas (SnH_4) is potentially the cause of this instability [22]. Tin droplet ejection has also been observed in plasma created from diatomic gasses other than hydrogen [17]. In that work, the hypothesis is that the plasma enhanced solubility [23] lead to the formation and supersaturation of gas molecules within the tin, which will then burst. Similar to KH and RT, this additional instability due to the chemical interaction between the hydrogen and tin could potentially be suppressed by reducing the pore size even more. As a result, the capillary pressure will increase and the gas bubbles will be physically constrained. Ou found that reducing the pore size from 800 to 104 µm already decreased the number of released droplets significantly. However, it still unclear how much further it can be reduced, once a critical value is reached it could potentially be fully suppressed [24]. Moreover, multiples manufacturing techniques are available to produce a CPS and its effect on surface stability is unclear.

2. Methodology

2.1. Targets, preparation, and wetting

Sintered stainless steel (s.s.) discs were used to determine the influence of pore size. This material was chosen as steel targets were readily available and already existed in a broad pore size range. The sintering process bonds steel powder into a porous structure where liquid tin can impregnate, an example of the microstructure is shown in Fig. 1. Nine discs (Mott Corporation) were used with a pore size between 0.5 and 100 µm. All discs have a diameter of 25.4 mm, but their heights varies, Table 1 shows the precise values. To compensate for the height difference, a solid s.s. disc was placed behind the targets, which ensured a similar target temperature during exposure.

Wettability is the tendency to form an interaction between a solid and a liquid such that the liquid is attached to the solid [25]. When s.s. or tungsten is exposed to ambient air, an oxide layer is formed, preventing wetting with tin [26,27]. This layer can be removed using vacuum brazing at high temperatures [26,28]. The oven used operates

at a pressure of 1 mPa. Initially, the temperature was set to 750 °C; however, an increase to first 900 °C and later 950 °C was necessary to wet all targets. Stainless steel cannot be used in a tokamak, due to its poor thermal conductivity, among other reasons. Instead, tungsten is the leading CPS material option. Three different types of W targets were therefore also investigated. Their wetting procedure is different, as some targets have been used before or were provided already wetted by different institutes. The targets and their wetting procedure are described next.

1. A sintered disc (Edgetech Industries) with a diameter of 39 mm ± 2 mm, a thickness of 3 mm ± 0.2 mm and a porosity between 0.50 and 0.55. The powder used for the manufacturing process has an average particle diameter of 4.5–6 µm. Since the manufacturer could not state the pore size, this was determined using backscatter electron mode (BSE) on the scanning electron microscopy (SEM), see Fig. 1. This figure is processed by binarization of the image using ImageJ [29] to determine the average hydraulic diameter of the voids, resulting in 0.65 µm ± 0.32 µm. Assumed is that there is no significant difference in the internal and external microstructure. Wetting performed in a setup at ASML allowed the filling of the target with 13.14 g. This setup consists of a vessel operated at a pressure of 16 Pa hydrogen, where a hydrogen radical load of 6×10^{17} at s^{-1} cm^{-2} is generated over a hot W-filament (1950 °C). Hydrogen was added to effectively remove tungsten oxides [30,31] and thus accelerate the wetting process. Tungsten oxides are removed from the target at temperatures > 700 °C within 30 min, after which the wetting and filling with liquid Sn is achieved at temperatures of 400–500 °C.

2. A 3D-printed target identical to that used in [32]. It has a height of 17 mm and a diameter of 24.5 mm. Grooves printed on the surface provide the CPS texture. The width of its grooves and thus its effective pore size is 100 µm ± 10 µm at the plasma facing surface (PFS). It was first cleaned using HCl (37%) and placed in a vacuum oven at 1 mPa and 1000 °C for 2 h to remove all prior traces of Li, oxides and other impurities. After this, it was wetted similarly to the sintered disc and filled with 3.33 g of Sn.

3. A wire felt with a diameter of 26 mm and a thickness of 3.3 mm. This design is similar to the limiter that has been used in Frascati Tokamak Upgrade (FTU), which had a pore size of 30 µm [13, 14]. The new felt has been produced with a reduced pore size using a pure W wire to obtain a compact knit. The effective pore size has been estimated in the order of one micron. After production, the felt has been cleaned using acetone and then placed in a vacuum oven at 1200 °C and 10^{-3} mPa for 1 h. Wetting was achieved by placing the CPS in a liquid tin pool, and using capillary action to fill the target.

All targets were mounted using a TZM clamping ring in Magnum-PSI, and four round witness plates (WPs) were positioned surrounding the targets. A layer of grafoil was placed between the target and the target holder. Fig. 2 shows an example where the 5 µm s.s. porous target is mounted. These WPs were used *ex-situ* to determine tin deposition close to the target and thus compare the Sn erosion from different

Table 2

Settings used in Magnum-PSI to expose various targets, with ion flux (Γ_i) and maximum heat flux (q_{max}). The witness plates on the s.s. targets have been changed twice, with the last WP used for both series 3 and 4.

Series	Target	$\Gamma_i [10^{23}\ \mathrm{m^{-2}}]$	$q_{max}[\mathrm{MW\,m^{-2}}]$	P [W]	WP
1	s.s.: all	0.65	1.5	105.4	changed
2	W: Sintered, 3D-printed and felt	14.37	5.6	959	changed
3	s.s. with pore size, 0.5,5,20 and $100\,\mu m$	1.89	1.9	201	not changed
4	s.s. with pore size, 0.5,5,20 and $100\,\mu m$	5.67	2.1	439	changed
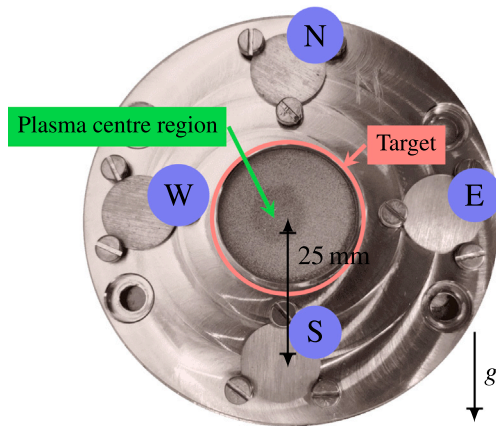
Fig. 2. Sintered s.s. target with a pore size of $5\,\mu m$ after plasma exposure in Magnum-PSI. The discolouration gives a reasonable indication of the central region of the plasma location. The letters in the blue circle indicate the cardinal position of the witness plates, where S is closer to the ground than N. (For interpretation of the references to colour in this figure legend, the reader is referred to the web version of this article.)
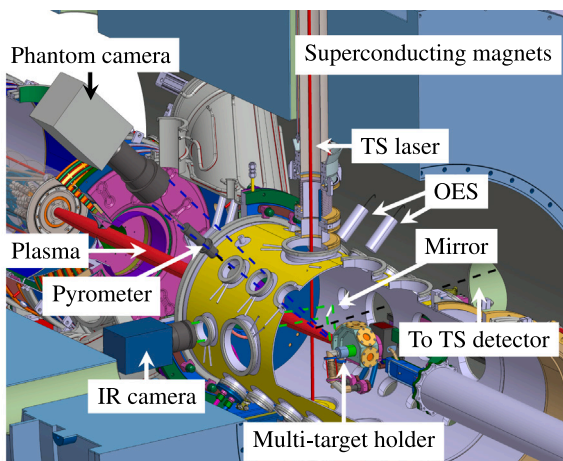
Fig. 3. Schematic overview of the relevant diagnostics in Magnum-PSI. The IR camera, the pyrometer, and the OES were all focussed viewing the front centre of the target, while the Phantom camera viewed tangentially to the target.

targets. The WPs are s.s. discs with a diameter of 12 mm and a thickness of 1 mm. They were placed at a radius of 25 mm from target centre to WP centre and are elevated 2 mm above the target, as can be seen in Fig. 2. Placing the 3D-printed target in a similar clamp as Fig. 2, had as result that the WPs are actually 10 mm below the target, since this target is thicker than the others.

2.2. Magnum-PSI

Both the s.s. and W targets were exposed for 10 s to the linear plasma device Magnum-PSI in DIFFER shown in Fig. 3. This device is capable of reaching ITER and DEMO relevant divertor plasma scenarios,

with a hydrogen flux of 10^{23}–$10^{25}\ \mathrm{m^{-2}\,s^{-1}}$ [33,34]. For this work, the magnetic field strength was varied between 0.4 and 0.6 T. The electron temperature and density were determined with Thomson scattering (TS) [35], positioned approximately 14 mm in front of the target. To enable TS measurements, an additional piece of glass was mounted on the window below the target as a precaution to prevent Sn droplets falling into the TS optics. The heat flux profile determined using the n_e and T_e obtained from TS was then used to obtain the maximum heat flux on the target. In this work T_e varied between 0.5–1.5 eV and n_e between 1–$50 \times 10^{19}\ \mathrm{m^{-3}}$. The total deposited power by the plasma was obtained using calorimetry [36]. A multiwavelength spectropyrometer (Far Associates FMPI-1) and an infrared (IR) camera (FLIR SC7000MB) measure the surface temperature. The single chord pyrometer was focused at the plasma beam spot centre (target centre) and used to calibrate the emissivity of the IR camera to determine the temperature of the target over the full surface. Furthermore, a fast visible light camera (Vision Research Phantom v12.1 camera) with a frame rate of 1 kHz and a resolution of $\approx 50\,\mu m$/pixel was positioned viewing tangentially to the surface of the target and was used to monitor any Sn droplets emerging from it. TRACK software (APREX solutions) allowed tracking of individual droplets over frames [37]. A second method to detect Sn was by using optical emission spectroscopy (OES) (Avantes AvaSpec-2048). The light intensity is measured for 30 s of which the first 10 s are from the plasma discharge. The last 5 s are considered to be a background noise. This is subtracted from the intensity measured during a shot. For a better comparison between series, the average integrated Gaussian tin peaks was normalized over the $H - \epsilon$ line (397.0 nm).

Plasma turbulence has been observed in linear plasma devices [38] and in Magnum-PSI this could be expected to drive MHD instabilities on the liquid surface [19]. However, cascaded arc sources have been shown to be highly quiescent [39], with density fluctuation levels up to two orders of magnitude lower than other type of arc sources [40]. Therefore, any potential influence of small scale turbulence on the plasma surface interaction is neglected in this study. In Magnum-PSI the neutral flux near the target only comes from volumetric recombination and target recycling when there is no gas puffing. Simulations in B2.5-Eunomia show that the neutral flux near the target is about 2 orders of magnitude lower compared to the H^+ flux [41]. Therefore, only the ion flux is considered to be a significant source of Sn droplet production.

2.3. Ion beam analysis

The WPs were examined ex-situ using Rutherford backscattering spectroscopy (RBS). The ion beam facility (IBF) at DIFFER hosts a singletron accelerator, which was used to accelerate $^4He^+$ to 2 MeV. Via steering and focusing magnets, the ion reaches a stand-alone Ion Beam Analysis Station (IBAS), where it hits the WPs and scatters on either tin or stainless-steel. A surface barrier detector measured the energy of the backscattered ions and were counted by a multichannel analyser. In the IBAS the incident angle $\alpha = 0°$, exit angle $\beta = 10°$ and scattering angle $\theta = 170°$. SIMNRA 7.03 was used to analyse the RBS data afterwards by adding layers with a certain thickness and fraction of Sn and Fe until it matches the experimental data [42]. In all other cases, the maximum layer thickness did not exceeded the recommended value from Resolnra [43]. In SIMNRA the particles × steradian were adjusted to the Fe substrate such that it agreed with the beam current. This was
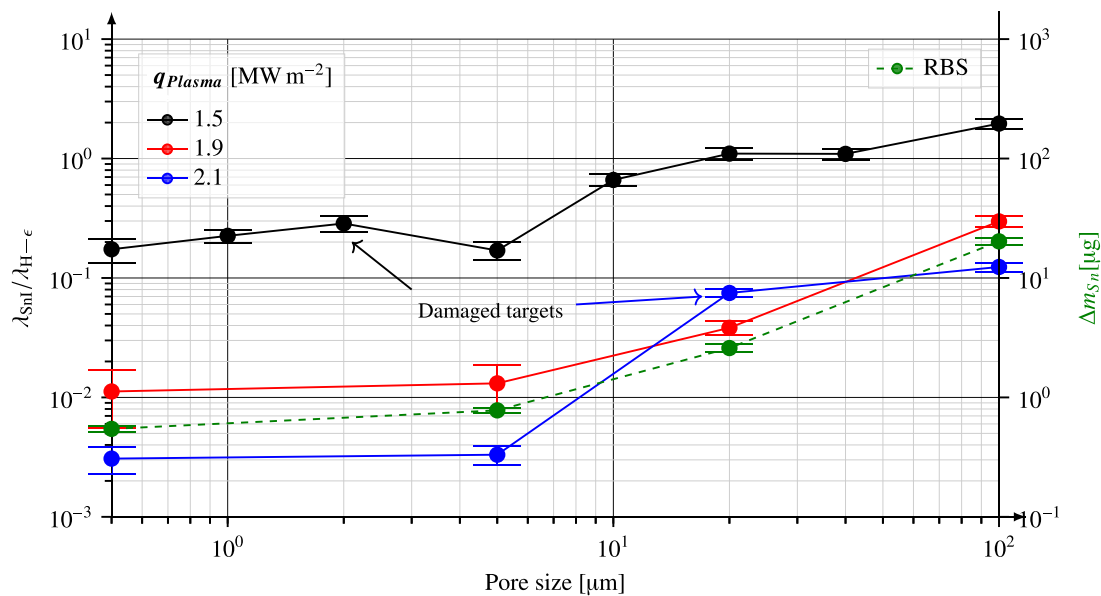
Fig. 4. Sn erosion measured on s.s. targets with a different pore size, when exposed to different heat fluxes in Magnum-PSI. The solid lines are the tin emission ($326.23\,\text{nm}$) normalized over hydrogen H-ϵ emission line. For the higher heat flux scenarios, the Balmer emission increased faster than the tin emission, hence the lower curve. The error bar in the graph is the covariance of the normalized Gaussian emission line. The dashed green line shows the total tin erosion measured by the RBS on the replaced WPs (i.e., $q = 1.9$ and $q = 2.1\,\text{MW}\,\text{m}^{-2}$). On all targets exposed to $q = 1.5\,\text{MW}\,\text{m}^{-2}$ no measurable Sn amount could be detected on the WPs using RBS($< 20\,\text{ng}$). Both the Sn emission and the Sn deposition on the WPs decrease a factor 50 when going from $100\,\mu\text{m}$ to $5\,\mu\text{m}$.

measured in the IBAS using a chopper wheel. The WPs surrounding the 3D-printed target were at different radial distance to the target compared to the others, since the 3D-printed target is thicker. To have a meaningful comparison between all targets, the total eroded mass $\Delta m_{Sn} = 2\pi R\bar{n}_{Sn}$ was determined, where R is the radius and $\bar{n}_{Sn}$ the average Sn atoms on the WPs per surface area. Where we assume that the evaporation is uniform over all angles. To determine the error in the RBS, the method of exact differentials is used. For the error in the counts, the Poisson noise is used.

3. Results and discussion

3.1. Sintered stainless-steel discs

A general overview of the experimental settings used is shown in Table 2. In the first series the temperature stayed below $900\,°\text{C}$ according to the pyrometer. In the third and fourth series, the temperature stayed below $1050\,°\text{C}$. During the first discharge, a crack of $\approx 1\,\text{cm}$ formed on the disc with a pore size of $2\,\mu\text{m}$, reaching from the centre towards the edge. The visible camera shows that the crack formed after about $4\,\text{s}$. Afterwards, the WPs were dismounted and fresh WPs were installed on the targets with a pore size of $0.5, 5, 20$ and $100\,\mu\text{m}$. Due to time constrains, only these were exposed a second and third time. The sintered s.s. disc with a pore size of $20\,\mu\text{m}$ broke during the last exposure. It was partly molten in the centre and a crack formed which extended from the centre to the edge of the disc. Visible camera video shows that this crack appearing within $2\,\text{s}$, though liquefying could not be directly observed. However, on the OES emission lines that can be attributed to Fe I [44] were visible from the first second. These emission lines were absent during all other measurements. Thermal contact might have been less for this target, explaining why it melted.

An appropriate Sn filter was not present for the high-speed camera during plasma exposure, therefore; some images became overexposed. From the s.s. targets, 0.5 and $20\,\mu\text{m}$ were overexposed during the third series and $5\,\mu\text{m}$ during the fourth series. In all other video images, the brightness was sufficient for analyses. Only in the third series on the $100\,\mu\text{m}$ two droplets were confirmed. In all cases, not a single droplet could be observed on the phantom camera. This implies that

any droplet emitted was too small to detect and thus has a maximum size of $50\,\mu\text{m}$. Typically, droplets are strongly heated by the plasma and glow brightly, and thus even smaller droplet may be expected to be visible. Fig. 4 shows the effect of pore size on the Sn erosion measured by the OES in the plasma and RBS on the WPs. On the OES, SnI emission could be observed at $317.51\,\text{nm}$ and $326.23\,\text{nm}$. Fig. 4 shows only the latter, but $317.51\,\text{nm}$ follows a similar trend. Using RBS, the total erosion yield is determined as in Section 2.3 and is also shown in Fig. 4. The result for the s.s. disc follows a similar trend as the OES. Both signals decrease a factor 50 when reducing the pore size from $100\,\mu\text{m}$ to $5\,\mu\text{m}$ and no further reduction below $5\,\mu\text{m}$ is observed. $20\,\mu\text{m}$ appears to be an outlier in the trend from the SnI emission for $q = 2.1\,\text{MW}\,\text{m}^{-2}$, which can be explained as the target was partly molten during exposure. It is therefore even more interesting that this could not be noted on the RBS. A possible explanation could be that the additional Sn was deposited closer to the target and could not reach the WPs. The target south from the sintered disc is not analysed, as it was used to explore the other options to measure tin deposition on the WP.

3.2. Tungsten targets

Table 3 shows the results for the tungsten targets and Fig. 5 shows a SEM image of the WPs. The droplets size on the WP are not necessary the same as they were in the plasma, as smaller droplet might have agglomerated. Most Sn erosion from tungsten targets was observed, on the 3D-printed target using both RBS and OES. This is understandable since the pore size is about two orders of magnitude higher than the other two. The W felts had a rather poor thermal connection to the heat sink. As a result, the temperature reached over $1300\,°\text{C}$, leading to significant Sn evaporation of $12\,\mu\text{g/s}$. On the fast imaging camera, most drops are observed with the sintered target, from which the droplet trace can be seen in Fig. 6. This despite having the smallest pore size, suggesting other factors are also important. On the visible camera, microscopic drops were observed on the PFS of both the sintered disc and the 3D-printed target. Overfilling of these targets could help explain these observations. When heating the W sintered disc target, Sn expands and could form a free surface layer at the PFS, from which tin can be ejected more easily. Tungsten surfaces exposed to

Table 3

Sn erosion from tungsten surfaces as observed by the OES during plasma exposure and RBS on the WPs. An abundance of emission lines were observed during the exposure of the W felts, most of which were saturated, hence the nan. This is most likely due to contamination of the target. The Phantom images in TRACK did show false positives; however, the exact number is unknown. Therefore, the number given in this table serves as an upper boundary.

W Target	Pore size [µm]	Δm_{Sn} [µg]	$\lambda_{SnI}/\lambda_{\zeta}$	T_{max} [°C]	Sn droplet Phantom camera [s^{-1}]
Felt	~ 1	33.8 ± 4.8	nan	1319 ± 3	< 1
Sintered	0.65 ± 0.32	13.7 ± 1.0	0.98 ± 0.20	1011 ± 2.7	< 375
3D-Printed	100 ± 10	331.2 ± 21.9	1.92 ± 0.21	1105 ± 1	< 20
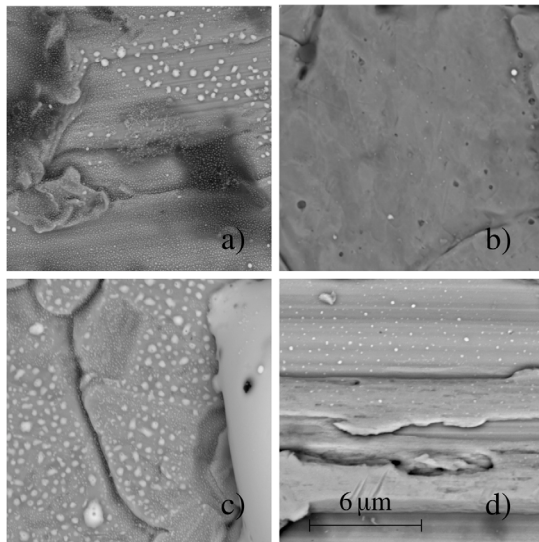
Fig. 5. Microscopic image from the WPs to the west of the targets. With (a) the s.s. 100 µm after the last series, (b) sintered W disc, (c) 3D-printed, (d) Felt. The brighter dots are Sn droplets, ranging from nano size covering s.s. 100 µm to the big drop on the right of the 3D-printed target. Sn droplets appear only occasionally for the sintered W disc. Observations of the SEM are inline with the RBS data shown in Fig. 4 and Table 3.
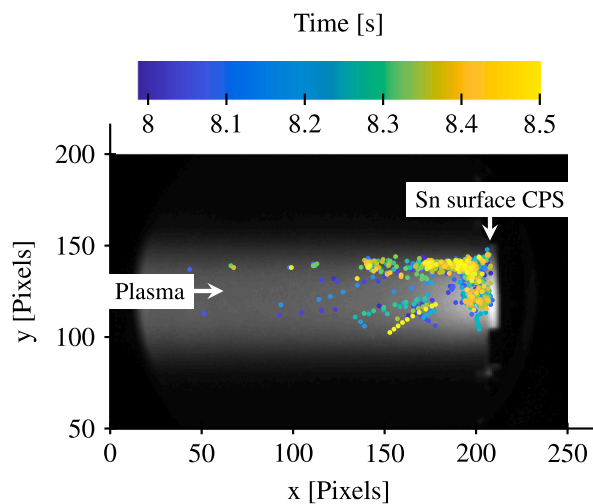
Fig. 6. Phantom image of the sintered tungsten target after 8.25 s, overlapping in colour are tin droplets traced using TRACK software at a certain time between 8 and 8.5 s. Droplets shows around $y \sim 150$ Pixels and $x > 150$ Pixels are mainly false positives. (For interpretation of the references to colour in this figure legend, the reader is referred to the web version of this article.)

the atmosphere will form a small oxide layer, reducing the wettability with Sn [45]. This was also observed when heating the sintered disc in a glovebox after exposure. Once the melting point had been reached, the disc started to "sweat" Sn droplets, rolling off the disc after scraping it with a knife. On Energy-dispersive X-ray spectroscopy (EDX) and SEM images made post-mortem on the sintered disc, only the tungsten structure could be observed similar to Fig. 1, leaving little to no traces of Sn. This means that Sn was so exceptionally confined in the disc that it does not form a coating on the outside of the CPS. Fortunately, hydrogen plasma can also remove oxides, although this takes time since a fluence of 5.58×10^{25} m^{-2} was required in previous research [45]. In these experiments, this would take about 40 s to be accumulated. With an increased exposure time, a conditioning effect would occur, but this needs to be confirmed in future experiments. The felts, on the other hand, were filled from the bottom using capillary forces, ensuring underfilling and the confined Sn always stuck to the W wires prior to the exposure. Therefore, tungsten was always wetted, and no macroscopic drops were formed.

In this work, the influence of tin droplets on the plasma parameters is not considered, which will be done in future research.

4. Conclusions and recommendations

Tin filled sintered stainless-steel targets with various pore sizes were exposed to Magnum-PSI. Rutherford backscattering and optical emission spectroscopy observed Sn erosion in the plasma and on nearby witness plates. They show that tin droplet ejection can effectively be reduced by decreasing the pore size of the CPS. Furthermore, different tungsten CPSs were exposed, 3D-printed, felts and sintered. Targets which were overfilled formed a pool of free surface tin on the plasma facing surface, enhancing the erosion yield. This because the size of hydrogen or stannane gas bubbles is no longer physically limited. It is therefore recommended to underfill a CPS with tin and leave internal space for thermal expansion. Furthermore, it is recommended to wet the CPS such that tungsten is not exposed to the atmosphere and oxidizes. These findings should ensure that a more effective CPS can be designed for future use with Sn.

CRediT authorship contribution statement

J.G.A. Scholte: Conceptualization, Methodology, Writing – original draft. **M. Iafrati:** Resources, Methodology. **S.S.H. Lam:** Methodology. **B. Tyburska-Pueschel:** Resources, Formal analysis. **M. Riepen:** Resources. **F. Brochard:** Formal analysis. **M.M.P. Vissers:** Resources. **T.W. Morgan:** Supervision.

Declaration of competing interest

Data availability

Data will be made available on request.

Acknowledgements

References

[1] J.H. You, G. Mazzone, E. Visca, H. Greuner, M. Fursdon, Y. Addab, C. Bachmann, T. Barrett, U. Bonavolontà, B. Böswirth, F.M. Castrovinci, C. Carelli, D. Coccorese, R. Coppola, F. Crescenzi, G. Di Gironimo, P.A. Di Maio, G. Di Mambro, F. Domptail, D. Dongiovanni, G. Dose, D. Flammini, L. Forest, P. Frosi, F. Gallay, B.E. Ghidersa, C. Harrington, K. Hunger, V. Imbriani, M. Li, A. Lukenskas, A. Maffucci, N. Mantel, D. Marzullo, T. Minniti, A.V. Müller, S. Noce, M.T. Porfiri, A. Quartararo, M. Richou, S. Roccella, D. Terentyev, A. Tincani, E. Vallone, S. Ventre, R. Villari, F. Villone, C. Vorpahl, K. Zhang, Divertor of the European DEMO: Engineering and technologies for power exhaust, Fusion Eng. Des. 175 (2022) 113010, http://dx.doi.org/10.1016/j.fusengdes.2022.113010.

[2] M.R. Gilbert, J.C. Sublet, Neutron-induced transmutation effects in W and W-alloys in a fusion environment, Nucl. Fusion 51 (4) (2011) http://dx.doi.org/10.1088/0029-5515/51/4/043005.

[3] R.A. Pitts, S. Carpentier, F. Escourbiac, T. Hirai, V. Komarov, S. Lisgo, A.S. Kukushkin, A. Loarte, M. Merola, A. Sashala Naik, R. Mitteau, M. Sugihara, B. Bazylev, P.C. Stangeby, A full tungsten divertor for ITER: Physics issues and design status, J. Nucl. Mater. 438 (SUPPL) (2013) S48–S56, http://dx.doi.org/10.1016/j.jnucmat.2013.01.008.

[4] J.P. Gunn, S. Carpentier-Chouchana, F. Escourbiac, T. Hirai, S. Panayotis, R.A. Pitts, Y. Corre, R. Dejarnac, M. Firdaouss, M. Kočan, M. Komm, A. Kukushkin, P. Languille, M. Missirlian, W. Zhao, G. Zhong, Surface heat loads on the ITER divertor vertical targets, Nucl. Fusion 57 (4) (2017) 046025, http://dx.doi.org/10.1088/1741-4326/aa5e2a.

[5] J. Linke, J. Du, T. Loewenhoff, G. Pintsuk, B. Spilker, I. Steudel, M. Wirtz, Challenges for plasma-facing components in nuclear fusion, Matter Radiat. Extrem. 4 (5) (2019) 056201, http://dx.doi.org/10.1063/1.5090100.

[6] G. Caruso, S. Ciattaglia, B. Colling, L.D. Pace, D.N. Dongiovanni, M. D'Onorio, M. Garcia, X.Z. Jin, J. Johnston, D. Leichtle, T. Pinna, M.T. Porfiri, W. Raskob, N. Taylor, N. Terranova, R. Vale, DEMO – the main achievements of the pre – concept phase of the safety and environmental work package and the development of the GSSR, Fusion Eng. Des. 176 (2022) 113010, http://dx.doi.org/10.1016/j.fusengdes.2022.113025.

[7] P. Rindt, J.L. van den Eijnden, T.W. Morgan, N.J. Lopes Cardozo, Conceptual design of a liquid-metal divertor for the European DEMO, Fusion Eng. Des. 173 (April) (2021) 046025, 112812, http://dx.doi.org/10.1016/j.fusengdes.2021.112812.

[8] G.G. Van Eden, T.W. Morgan, D.U. Aussems, M.A. Van Den Berg, K. Bystrov, M.C. Van De Sanden, Self-regulated plasma heat flux mitigation due to liquid Sn vapor shielding, Phys. Rev. Lett. 116 (13) (2016) 1–5, http://dx.doi.org/10.1103/PhysRevLett.116.135002.

[9] V.P. Budaev, I.E. Lyublinsky, S.D. Fedorovich, A.V. Dedov, A.V. Vertkov, A.T. Komov, A.V. Karpov, Y.V. Martynenko, G. Van Oost, M.K. Gubkin, M.V. Lukashevsky, A.Y. Marchenkov, K.A. Rogozin, G.B. Vasiliev, A.A. Konkov, A.V. Lazukin, A.V. Zakharenkov, Z.A. Zakletsky, Impact of liquid metal surface on plasma-surface interaction in experiments with lithium and tin capillary porous systems, Nucl. Mater. Energy 25 (2020) 100834, http://dx.doi.org/10.1016/j.nme.2020.100834.

[10] T.W. Morgan, A. Vertkov, K. Bystrov, I. Lyublinski, J.W. Genuit, G. Mazzitelli, Power handling of a liquid-metal based CPS structure under high steady-state heat and particle fluxes, Nucl. Mater. Energy 12 (2017) 210–215, http://dx.doi.org/10.1016/j.nme.2017.01.017.

[11] P. Rindt, The potential of liquid-metal 3D-printed heat shields for fusion reactors (Ph.D. thesis), Eindhoven University of Techology, 2019, URL https://research.tue.nl/en/publications/the-potential-of-liquid-metal-3d-printed-heat-shields-for-fusion-.

[12] R. Dejarnac, J. Horacek, M. Hron, M. Jerab, J. Adamek, S. Atikukke, P. Barton, J. Cavalier, J. Cecrdle, M. Dimitrova, E. Gauthier, M. Iafrati, M. Imrisek, A. Marin Roldan, G. Mazzitelli, D. Naydenkova, A. Prishvitcyn, M. Tomes, D. Tskhakaya, G. Van Oost, J. Varju, P. Veis, A. Vertkov, P. Vondracek, V. Weinzettl, Overview of power exhaust experiments in the COMPASS divertor with liquid metals, Nucl. Mater. Energy 25 (2020) 100801, http://dx.doi.org/10.1016/j.nme.2020.100801.

[13] G. Mazzitelli, M.L. Apicella, M. Iafrati, G. Apruzzese, F. Crescenzi, L. Gabellieri, A. Mancini, M. Marinucci, A. Romano, Experiments on FTU with a liquid tin limiter, Nucl. Fusion 59 (9) (2019) 096004, http://dx.doi.org/10.1088/1741-4326/ab1d70.

[14] A. Vertkov, I. Lyublinski, M. Zharkov, G. Mazzitelli, M.L. Apicella, M. Iafrati, Liquid tin limiter for FTU tokamak, Fusion Eng. Des. 117 (2017) 130–134, http://dx.doi.org/10.1016/j.fusengdes.2017.01.041.

[15] I.E. Lyublinski, A.V. Vertkov, M.Y. Zharkov, S.V. Mirnov, V.A. Vershkov, Y.V. Glazyuk, G.E. Notkin, S.A. Grashin, A.Y. Kislov, A.T. Komov, Complex of lithium and tungsten limiters for 3 MW of ECR plasma heating in T-10 tokamak. Design, first results, Nucl. Fusion 57 (6) (2017) 066006, http://dx.doi.org/10.1088/1741-4326/aa65e9.

[16] T.W. Morgan, P. Rindt, G.G. Van Eden, V. Kvon, M.A. Jaworksi, N.J. Cardozo, Liquid metals as a divertor plasma-facing material explored using the pilot-PSI and Magnum-PSI linear devices, Plasma Phys. Control. Fusion 60 (1) (2018) 014025, http://dx.doi.org/10.1088/1361-6587/aa86cd.

[17] W. Ou, F. Brochard, T.W. Morgan, Bubble formation in liquid Sn under different plasma loading conditions leading to droplet ejection, Nucl. Fusion 61 (6) (2021) 066030, http://dx.doi.org/10.1088/1741-4326/abf9e0.

[18] G.V. Miloshevsky, A. Hassanein, Modelling of Kelvin-Helmholtz instability and splashing of melt layers from plasma-facing components in tokamaks under plasma impact, Nucl. Fusion 50 (11) (2010) 115005, http://dx.doi.org/10.1088/0029-5515/50/11/115005.

[19] M.A. Jaworski, T. Abrams, J.P. Allain, M.G. Bell, R.E. Bell, A. Diallo, T.K. Gray, S.P. Gerhardt, R. Kaita, H.W. Kugel, B.P. Leblanc, R. Maingi, A.G. McLean, J. Menard, R. Nygren, M. Ono, M. Podesta, A.L. Roquemore, S.A. Sabbagh, F. Scotti, C.H. Skinner, V.A. Soukhanovskii, D.P. Stotler, Liquid lithium divertor characteristics and plasma-material interactions in NSTX high-performance plasmas, Nucl. Fusion 53 (8) (2013) 083032, http://dx.doi.org/10.1088/0029-5515/53/8/083032.

[20] R. Hutschemakers, R. Jaspers, G. Rooij, J. van den Berg, Determination of the rotational velocity profiles in Magnum-PSI using a spectrometer for improvement of B2.5-Eunomia, Student Thesis: Master, Eindhoven university of technology, 2020, URL https://pure.tue.nl/ws/portalfiles/portal/150975810/0808235_Hutschemakers_R.W.H._Msc._Thesis.pdf.

[21] A.E. Shumack, V.P. Veremiyenko, D.C. Schram, H.J. De Blank, W.J. Goedheer, H.J. Van Der Meiden, W.A. Vijvers, J. Westerhout, N.J. Lopes Cardozo, G.J. Van Rooij, Rotation of a strongly magnetized hydrogen plasma column determined from an asymmetric Balmer-β spectral line with two radiating distributions, Phys. Rev. E - Stat. Nonlinear Soft Matter Phys. 78 (4) (2008) 046405, http://dx.doi.org/10.1103/PhysRevE.78.046405.

[22] A. Manhard, T. Schwarz-Selinger, M. Balden, T. Durbeck, H. Maier, R. Neu, Deuterium retention in solid and liquid tin after low-temperature plasma exposure, Nucl. Fusion 60 (10) (2020) 106007, http://dx.doi.org/10.1088/1741-4326/aba801.

[23] K. Mundra, T. Debroy, A general model for partitioning of gases between a metal and its plasma environment, Metall. Mater. Trans. B 26 (1) (1995) 149–157, http://dx.doi.org/10.1007/BF02648987.

[24] S.F. Jones, G.M. Evans, K.P. Galvin, Bubble nucleation from gas cavities - a review, Adv. Colloid Interface Sci. 80 (1) (1999) 27–50, http://dx.doi.org/10.1016/S0001-8686(98)00074-8.

[25] D. Bonn, J. Eggers, J. Indekeu, J. Meunier, Wetting and spreading, Rev. Modern Phys. 81 (2) (2009) 739–805, http://dx.doi.org/10.1103/RevModPhys.81.739.

[26] O. Kozlova, R. Voytovych, M.F. Devismes, N. Eustathopoulos, Wetting and brazing of stainless steels by copper-silver eutectic, Mater. Sci. Eng. A 495 (1–2) (2008) 96–101, http://dx.doi.org/10.1016/j.msea.2007.10.101.

[27] N. Eustathopoulos, M.G. Nicolas, B. Drevet (Eds.), Chapter 5 wetting properties of metal/metal systems, in: Wettability At High Temperatures, in: Pergamon Materials Series, vol. 3, Pergamon, 1999, pp. 175–197, http://dx.doi.org/10.1016/S1470-1804(99)80007-8.

[28] Y. Arata, A. Ohmori, H.F. Cai, Studies on vacuum brazing (Report II) : Removal of oxide film from stainless steel surface and brazing alloy spreading mechanism(welding physics, process & instrument), Trans. JWRI 12 (1) (1983) 27–34, URL http://hdl.handle.net/11094/9193.

[29] T. Ferreira, W. Rasband, Imagej user guide, in: IJ 1.46r Revised Edition, 2012, URL https://imagej.nih.gov/ij/docs/guide/user-guide.pdf.

[30] J.O. Hougen, R.R. Reeves, G.G. Mannella, Reduction of Tungsten oxides with hydrogen, Ind. Eng. Chem. 48 (2) (1956) 318–320, http://dx.doi.org/10.1021/ie50554a042.

[31] T. Zimmerl, W.D. Schubert, A. Bicherl, A. Bock, Hydrogen reduction of tungsten oxides: Alkali additions, their effect on the metal nucleation process and potassium bronzes under equilibrium conditions, Int. J. Refract. Met. Hard Mater. 62 (2017) 87–96, http://dx.doi.org/10.1016/j.ijrmhm.2016.06.015.

[32] P. Rindt, J. Mata González, P. Hoogerhuis, P. Van Den Bosch, M. Van Maris, D. Terentyev, C. Yin, M. Wirtz, N.J. Lopes Cardozo, J.A. Van Dommelen, T.W. Morgan, Using 3D-printed tungsten to optimize liquid metal divertor targets for flow and thermal stresses, Nucl. Fusion 59 (5) (2019) 054001, http://dx.doi.org/10.1088/1741-4326/ab0a76.

[33] H.J. Van Eck, T. Abrams, M.A. Van Den Berg, S. Brons, G.G. Van Eden, M.A. Jaworski, R. Kaita, H.J. Van Der Meiden, T.W. Morgan, M.J. Van De Pol, J. Scholten, P.H. Smeets, G. De Temmerman, P.C. De Vries, P.A. Zeijlmans Van Emmichoven, Operational characteristics of the high flux plasma generator Magnum-PSI, Fusion Eng. Des. 89 (9–10) (2014) 2150–2154, http://dx.doi.org/10.1016/j.fusengdes.2014.04.054.

[34] G. De Temmerman, M.A. Van Den Berg, J. Scholten, A. Lof, H.J. Van Der Meiden, H.J. Van Eck, T.W. Morgan, T.M. De Kruijf, P.A. Zeijlmans Van Emmichoven, J.J. Zielinski, High heat flux capabilities of the Magnum-PSI linear plasma device, Fusion Eng. Des. 88 (6–8) (2013) 483–487, http://dx.doi.org/10.1016/j.fusengdes.2013.05.047.

[35] H.J. Van Eck, T.A. Hansen, A.W. Kleyn, H.J. Van Der Meiden, D.C. Schram, P.A. Zeijlmans Van Emmichoven, A differentially pumped argon plasma in the linear plasma generator Magnum-PSI: Gas flow and dynamics of the ionized fraction, Plasma Sources. Sci. Technol. 20 (4) (2011) 045016, http://dx.doi.org/10.1088/0963-0252/20/4/045016.

[36] H.J. Van Eck, A.W. Kleyn, A. Lof, H.J. Van Der Meiden, G.J. Van Rooij, J. Scholten, P.A. Zeijlmans Van Emmichoven, Divertor conditions relevant for fusion reactors achieved with linear plasma generator, Appl. Phys. Lett. 101 (22) (2012) 224107, http://dx.doi.org/10.1063/1.4768302.

[37] R. Baude, M. Desecures, Track software, URL http://www.aprexsolutions.com.

[38] V.P. Budaev, S. Takamura, N. Ohno, S. Masuzaki, Superdiffusion and multifractal statistics of edge plasma turbulence in fusion devices, Nucl. Fusion 46 (4) (2006) S181–S191, http://dx.doi.org/10.1088/0029-5515/46/4/S10.

[39] M. Yoshikawa, H.V.D. Meiden, R. Al, K. Bystrov, J. Vernimmen, J. Kohagura, Y. Shima, X. Wang, M. Ichimura, M. Sakamoto, Y. Nakashima, Preliminary measurements of low frequency fluctuations by a microwave interferometer system and a fast camera in Pilot-Psi device, Plasma Fusion Res. 10 (2015) 1202088–1202088, http://dx.doi.org/10.1585/pfr.10.1202088.

[40] Y. Hayashi, K. Ješko, H.J. Van Der Meiden, J.W. Vernimmen, T.W. Morgan, N. Ohno, S. Kajita, M. Yoshikawa, S. Masuzaki, Plasma detachment study of high density helium plasmas in the Pilot-PSI device, Nucl. Fusion 56 (12) (2016) 126006, http://dx.doi.org/10.1088/0029-5515/56/12/126006.

[41] R. Chandra, H.J. de Blank, P. Diomede, H.J.N. van Eck, H.J. van der Meiden, T.W. Morgan, J.W.M. Vernimmen, E. Westerhof, B2.5-Eunomia simulations of Magnum-PSI detachment experiments: I. quantitative comparisons with experimental measurements, Plasma Phys. Control. Fusion 63 (9) (2021) 095006, http://dx.doi.org/10.1088/1361-6587/ac11b6.

[42] M. Mayer, SIMNRA User's Guide, Tech. rep., Max-Planck-Institut für Plasmaphysik, 2020, p. 369, URL https://mam.home.ipp.mpg.de/Version7.html.

[43] M. Mayer, RESOLNRA: A new program for optimizing the achievable depth resolution of ion beam analysis methods, Nucl. Instrum. Methods Phys. Res. Sect. B: Beam Interactions Mater. Atoms 266 (8) (2008) 1852–1857, http://dx.doi.org/10.1016/j.nimb.2007.11.071.

[44] NIST: Atomic Spectra Database Lines Form, URL https://physics.nist.gov/PhysRefData/ASD/lines_form.html.

[45] P. Rasulyaar, Reduction of tungsten oxide using a hydrogen plasma, Eindhoven university of technology, 2021, URL https://research.tue.nl/en/studentTheses/reduction-of-tungsten-oxide-using-a-hydrogen-plasma.